www.czasopisma.pan.pl PAN www.journals.pan.pl

ARCHIVES of FOUNDRY ENGINEERING

ISSN (2299-2944)
Volume 21
Issue 2/2021

17 – 28

10.24425/afe.2021.136093

3/2

Published quarterly as the organ of the Foundry Commission of the Polish Academy of Sciences

Spatial Thermo-Mechanical Model of Mushy Steel Deformation Based on the Finite Element Method

M. Hojny *, T. Dębiński, M. Głowacki, Trang Thi Thu Nguyen
AGH University of Science and Technology, Cracow, Poland
* Corresponding author. E-mail address: mhojny@metal.agh.edu.pl

Received 09.12.2020; accepted in revised form 02.04.2021

Abstract

The paper reports the results of work leading to the construction of a spatial thermo-mechanical model based on the finite element method allowing the computer simulation of physical phenomena accompanying the steel sample testing at temperatures that are characteristic for the soft-reduction process. The proposed numerical model is based upon a rigid-plastic solution for the prediction of stress and strain fields, and the Fourier-Kirchhoff equation for the prediction of temperature fields. The mushy zone that forms within the sample volume is characterized by a variable density during solidification with simultaneous deformation. In this case, the incompressibilitycondition applied in the classic rigid-plastic solution becomes inadequate. Therefore, in the presented solution, a modified operator equation in the optimized power functional was applied, which takes into account local density changes at the mechanical model level (the incompressibility condition was replaced with the condition of mass conservation). The study was supplemented withexamples of numerical and experimental simulation results, indicating that the proposed model conditions, assumptions, and numerical models are correct.

Keywords: Mechanical properties, Soft-reduction, Semi-solid, Numerical modelling, Physical simulation

1. Introduction

The intensive development of methods and techniques in virtual engineering and manufacturing allows engineers to apply an innovative approach to issues related to designing new processes. In recent years, there has been an intensive development of integrated casting and rolling of slabs, especially with the mushy core [1,2]. Compared to conventional hot rolling, the process of rolling slabs with the semi-solid core is competitive both in the environmental (reduction of noxious gases and dust) and economical (reduction of energy consumption) aspects. The use of modern Gleeble thermo-mechanical simulators allowsfor a selected manufacturing process to be physically simulated.It means that the changes in, for example, temperature or strain, to which the test material is subjected in an actual manufacturing process, are reproduced in laboratory conditions. Small samples (cylindrical and cuboidal) made of the same material that is applied in the actual manufacturing process are used in the tests. They are subjected to various variants of physical simulation to assess their thermal-mechanical properties, which consequently allows the process guidelines to be developed, subsequently enabling the estimation of optimal operating parameters of equipment in the process line designed. This approach enables theexperimental results to be directly transferred to industrial practice. On the other hand, the formulated numerical models of high-temperature steel processing can be provisionally verified in laboratory conditions. At the same time, the simulation enableshigh-temperature process engineering to be aided by

reducing the designing time and costs of experiment execution. A numerical model of high-temperature steel processing should include effects appropriate for this temperature range (solidification, variable density) [3,4]. The existence of an adequate rheological model is a relevant aspect for the result of a numerical simulation [3,5]. Thermal effects, such as heat generation and flow, heat exchange with the environment, or the accumulation and formation of internal stress during solidification with simultaneous deformation are the final factors [4]. To obtain a comprehensive description of the behavior of steel deformed within temperature ranges near the solidus line, a 3D mathematical model needs to be formulated. It arises from the fact that the mushy zone often has an irregular shape. It is clear that now the most important problem related to the modeling of the deformation behavior of semi-solid steel is a lack of appropriate extra-high thermal-physical and mechanical properties. It should be emphasized that not much information concerning the material state, in particular for steel, can be found in the available literature. Reviewing the industry literature from the last decade, we can find many items wherein the authors focused on experimental research [6,7,8]. Many references also containthe results of studies related to the numerical modeling of heating or deforming non-ferrous metal alloys [9,10,11]. The first findings of studies concerning the high-temperature processing of steel were presented in recent years [12-17]. The main factor influencing this fact is the high value of the solidus temperature of steel compared to non-ferrous metals. Therefore, it was easier to conduct experiments related to the high-temperature deformation of non-ferrous metals in laboratory conditions. In recent years, the intensive development of integrated metallurgical processes combined with rolling a product to the final dimensions and shape has been observed [18]. Very often, final product quality problems occur during the production cycle, in particular when casting new steel grades. The occurring temperature ranges with reduced workability are amongthe most frequent reasons of failures. If, during the cast strand straightening operation, its surface (or edge) temperature is within the cast steel reduced workability range, there is a high likelihood of crack initiation in the strand cast. Figure1 showsa diagram of the continuous casting process with marked critical process stages where either internal or frontal cracks can be initiated.

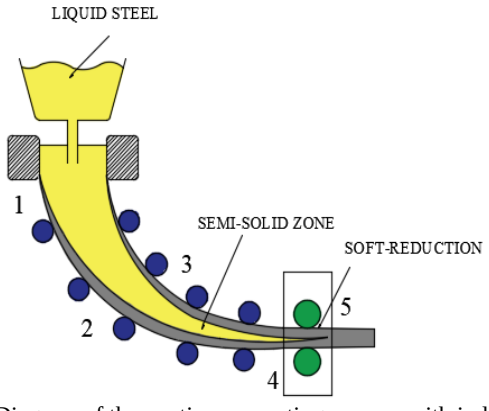

Fig. 1. Diagram of the continuous casting process with indicated critical process stages (1-5) where either internal or frontal cracks can be initiated

The cast strand area immediately after leaving the mold (1), the strand bending (2-3), and the straightening stage (4) can be classified as critical stages. The area of strong tensile stress (5) is a critical stage for particular roller pressure installations, the so-called soft-reduction system [19,20]. Knowing the mechanical properties of steel at temperature ranges close to the solidus line, and in particular the ranges of reduced plasticity, we can effectively control the steel casting process to prevent cracking, etc.On the other hand, the continuously growing research capabilities of Gleeble thermal-mechanical simulators and their increasingly widespread use have allowed research work on the experimental deformation of semi-solid steel strands to be conductedon the laboratory scale [21]. Comprehensive solutions concerning the modeling of semi-solid steel processing (heating, melting, and deformation) in the experimental research area and the development of new numerical models are missing in the literature.

This was the author's main motivation to commence work related to the development of innovative numerical models and methods of a high-temperature experiment in the context of aiding the engineering of new continuous casting processes, in particular the numerical simulation of the soft-reduction process.Therefore, the main objective of the presentpaper was to develop a spatial thermo-mechanical model based on the finite element method allowing the computer simulation of physical phenomena accompanying the steel sample testing at temperatures that are characteristic for the soft-reduction process. The developed solution combines the testing capabilities of modern Gleeble simulators with the author's original simulation software, called DEFFEM 3D [3,22], which was applied for the numerical implementation of the mathematical models presented in the paper.

A modified rigid-plastic model presented in the paper is a unique solution.where local variations of density of the medium subjected to deformation during its simultaneous solidification were included at the mechanical model level. Computer-aided physical simulations enable the high-temperature mechanical properties of the steel tested to be determined. At the same time, the findings obtained by conducting high-temperature experiments are a unique foundation for the qualitative verification of the formulated numerical model.The developed model was practically utilized in implementation projects (aerospace) when developing a new process for hot forming aircraft engine parts [23] (resistance heating of the blank) or a welding technology for aircraft engine assemblies to minimize deformations during the welding process [24] (prediction high-temperature stress-strain curves). Hot forging or semi-solid forging processes can be examples of other practical applications of the developed model [25,26]. The optimization of the above-mentioned processes may be focused on simplifying or eliminating some process operations. The final result is a significant reduction of manufacturing costs and energy consumption (forging in the semi-solid state compared to the classic hot forging process). Most importantly, by reducing noxious dust and gas emissions, the developed and continuously improvingprocesses will be more environmentally friendly.

2. Extra-high temperature experiments

The experiments for the verification of the mathematical model were conducted using the testing capabilities of a Gleeble 3800 thermal-mechanical simulator. Low carbon steel S355 was the material selected for the tests. The chemical composition is shown in Table 1.

Table 1.
Mass percentage of the elements in the investigated low carbon steel S355

C	Mn	Si	P	S	Cr	Ni
0.16	1.26	0.26	0.011	0.009	0.14	0.06

The solidus and liquidus temperatures are 1,465°C and 1,513°C, respectively. Hexahedral samples, with dimensions 10x10x100 mm (denoted as type B) and cylindrical samples, with dimensions Ø10 x 124 mm (denoted as type D), were used in the tests. Figure 2 shows a view of the chamber of the Gleeble 3800 thermal-mechanical simulator system with a D-type sample mounted in copper grips. In addition, in a test with the D-type sample, a quartz shield was used in the area of sample melting [3].

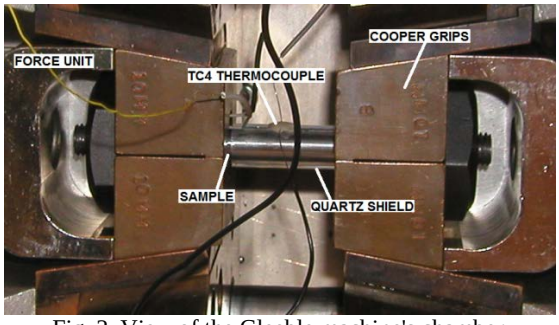

Fig. 2. View of the Gleeble machine's chamber (Hydrawedge unit)

Figure 3 shows diagrams of the samples used in the tests including the positions of thermocouples and locations of heat transfer areas. The achieved lengths of free zones for the samples of type B and D were 67 and 39.5 (mm), respectively. For the D-type samples we can define five heat transfer zones, denoted from Z1 to Z5, respectively (Fig. 3-A). The sample areas denoted as Z2 and Z4 present the contact zones of the tested sample and the grips. In the numerical modeling context, these are the key areas where intensive heat transfer to the tool occurs. Zones Z1, Z3, and Z5 define the sample areas where free heat transfer to the environment occurs. In the test variant with B-type samples, three heat transfer zones can be defined, denoted from Z1 to Z3, respectively (Fig. 3-B). The sample areas denoted as Z1 and Z3 present the contact zones of the sample and the grips. The free zone of the sample was denoted as Z2. The location of the actual thermocouple TC4 is equivalent to the numerical sensor NTC4 in the numerical model.

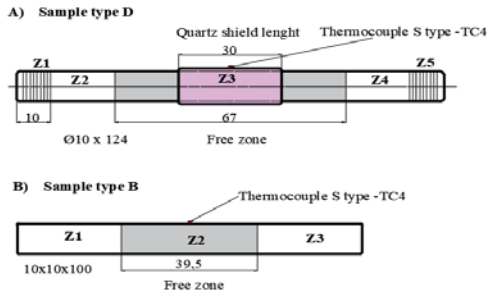

Fig. 3. Diagrams of the samples used in the experiments indicating the heat transfer zones (Z1-Z5)

A two-stage experiment was proposed:

1) The objective of the first stage was to provide the data necessary to develop the stress-strain relationship for numerical simulation. In the tests, cylindrical samples were used (type D).
2) The objective of the second stage was to experimentally verify the formulated 3D thermal-mechanical model for the correctness of the estimation of the geometrical size of the deformation zone. In the tests, hexahedral samples were used (type B).

The experiment program for the 1st and 2nd stage is shown in Table 2 and Table 3, respectively.

Table 2.
The test program applied during the 1st stageof the experiment

HEATING PROCESS			
	Heating temperature, [°C]	Heating rate, [°C/s]	Holding time, [s]
I	1420	20	–
II	1460	1	60
DEFORMATION PARAMETERS - TENSILE TESTS			
Cooling rateto deformation temperature,[°C/s]		Holding time, [s]	
10		10	
Deformation temperature range: from 400°C to 1,450°C			
Stroke: 2 mm			
Stroke rate: 1 and 20 mm/s			

Table 3.
The test program applied during the 2nd stage of the experiment

HEATING PROCESS			
	Heating temperature, [°C]	Heating rate, [°C/s]	Holding time, [s]
I	1400	20	–
II	1450	1	10
DEFORMATION PARAMETERS - TENSILE TESTS			
Cooling rateto deformation temperature, [°C/s]		Holding time, [s]	
10		–	
Deformation temperature range: from 1,200°C to 1,435°C			
Stroke: 5 mm			
Stroke rate: 1 mm/s			

At both stages, the characteristic of the current intensity versus the time was also recorded (Fig. 4). It was a necessary input to perform the resistance heating simulation in accordance with the formulated model presented hereinafter.

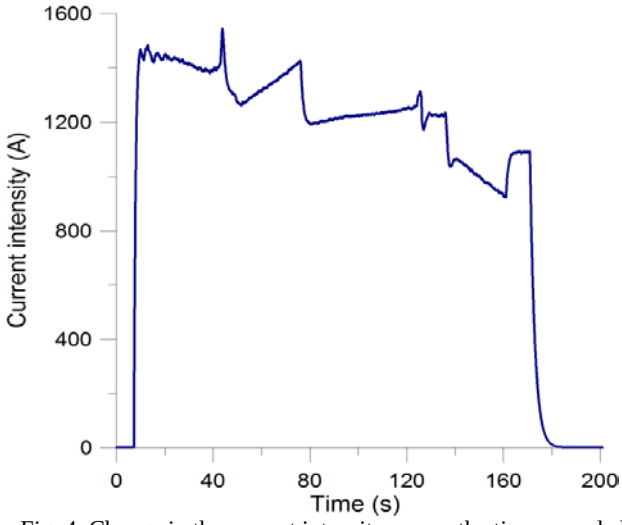

Fig. 4. Change in the current intensity versus the time recorded during the experiment (sample type B)

3. Mathematical model

The mathematical model is based on a rigid-plastic approach for predicting stress and strain fields, and the solution of the Fourier-Kirchhoff equation for predicting temperature fields. The application of the rigid-plastic model is becoming more and more important for high-temperature processes. As shown by the tests conducted in conditions of hot deformation, the impact of elastic strain on the strain tensor components is negligible [27]. For processes occurring in the temperature ranges close to the solidus line, elastic strains are even less important. The application of the elastic-plastic medium model causes many difficulties when analyzing metal plastic working processes. This approach requires calculations of displacements, strains, and stress within the elastic range, and checking if a given element, previously elastic, has achieved the plastic flow state. Another difficulty is related to the impossibility of using large strain increments, which are concerned in the plastic working processes at extra-high temperatures. Therefore, adopting a rigid-plastic model allows us to avoid the foregoing difficulties, and allows large strain increments to be analyzed, while ensuring the adequate accuracy of the solution. The algorithm of the proposed solution is based on the optimization of the power functional. It comprises three main terms according to the equation (1) [3,28,29]:

$$W = \dot{W}_\sigma + \dot{W}_\lambda + \dot{W}_t \tag{1}$$

The first part in equation (1) is the plastic strain power $\dot{W}_\sigma$, the second is the power necessary to change the volume of the continuous medium $\dot{W}_\lambda$, and the last one is the friction power $\dot{W}_t$. Adapting the solution to the test conditions in the Gleeble unit, the third term in equation (1) can be neglected. It arises from the fact that the sample is held tightlyin the simulator tools and friction can be neglected. Therefore, after this simplification, the equation (1) takes the form:

$$J = \dot{W}_p + \dot{W}_\lambda \tag{2}$$

The rigid-plastic formulation requires taking into account the condition of mass conservation within the deformation zone. For the deformation of solids and liquids with constant density, this condition may be simplified to the condition of incompressibility. This condition is usually satisfied with adequate accuracy during the optimization of the power functional J [27]. In most of the solutions applied, there is a slight, but noticeable loss of volume, which is caused by the incomplete meeting of the condition imposed on the solution in the numerical form [3]. The change in the deformation zone volume is negligible in computer simulations of traditional rolling processes, although, in some more accurate solutions, the methods of restoring the volume of the metal deformed are applied [27]. There is a different situation when we deal with materials in a semi-solid state. Their density varies during the process, and these changes cause a natural, physically justified change in the volume of a body with a constant mass. The amount of the volume loss caused by numerical errors is comparable with the changes caused by fluctuations in material density. There is another problem specific to a variable density of a continuum. This is the power $\dot{W}_\lambda$, present in function (2), applied in most solutions, which significantly contributes to the total power. Even if the iterative process is coming to the end, this power is significant, in particular, if we deal with an insufficient convergence of optimization procedures, which is often the case [3,27]. If, for the area discretization we focus exclusively on the power $\dot{W}_\lambda$, a number of possible optimal solutions appear which are related to the possible directions and velocities of movement of discretization nodes so that the volume of the deformed zone is maintained. Each of such solutions creates a local optimum for power $\dot{W}_\lambda$, and, therefore, for the whole functional (2). This makes the functional optimization difficult because of the lack of explicit direction of changes of the total power value for the global solution. A change in the material density also hinders optimization, particularly as the condition of constant volume ceases to apply and should be replaced with a full condition of mass conservation.

For the spatial strain state, the condition of incompressibility will be described by a differential equation specific to this state [28,29]:

$$\frac{\partial v_x}{\partial x} + \frac{\partial v_y}{\partial y} + \frac{\partial v_z}{\partial z} = 0 \tag{3}$$

where: (v_x, v_y, v_z) are the components of the velocity vector in the Cartesian coordinate system.For zones with a variable density, the equation (3) is replaced by the condition of mass conservation in the form [3,30]:

$$\frac{\partial v_x}{\partial x} + \frac{\partial v_y}{\partial y} + \frac{\partial v_z}{\partial z} - \frac{1}{\rho}\frac{\partial \rho}{\partial \tau} = 0 \tag{4}$$

where: ρ – density, τ – time.

Therefore, the work related to the failure to meet the condition of mass conservation is described by the equation [3,30]:

$$\dot{W}_\lambda = \int_V \lambda \left(\frac{\partial v_x}{\partial x} + \frac{\partial v_y}{\partial y} + \frac{\partial v_z}{\partial z} - \frac{1}{\rho}\frac{\partial \rho}{\partial t} \right) dV \tag{5}$$

In equation (5), λ is a penalty factor. Power $\dot{W}_\lambda$ in the computing process performs the function of penalty for not meeting the condition of incompressibility and during optimizing calculations it approaches zero. As aforementioned, density is one of the essential properties of semi-solid steel that most significantly influences the results of the computer simulation of its deformation. Changes in steel density in the mushy zone strictly depend on the porosity of the metallic structure. The variability of this parameter over time is very important for the computer simulation of the process concerned. The variations of density are caused by three primary effects: formation of the solid phase, laminar flow of the liquid phase through the porous area, and thermal shrinkage. The dependence of density changes on the metal velocity field and temperature significantly complicates the problem of the metal flow velocity field optimization. The coupled solution is difficult and very often a non-coupled model is used in the solutions applied. Therefore, an empirical model was used in the solution presented, where density only depends on temperature [3].The mechanical model has been coupled with the solution of the Fourier-Kirchhoff equation [3,28,29]:

$$\nabla^T (k \nabla T) + Q = c_p \rho \frac{\partial T}{\partial \tau} \tag{6}$$

where: k – thermal conductivity, Q – volume heat source, c_p– specific heat, ρ – density, τ – time.

Table 4.
Thermal-physical properties of the steel tested

Temp. (°C)	**Density** (g/cm^3)	**Specific heat** (J/(g K)	**Latent heat** (J/g)	**Enthalpy** (J/g)	**Resistivity** (10e-6 Ohm m)	**Conductivity** (W/(m K)
1520	6.97717	0.81806		1275.71312	1.31344	33.44813
1513.7	6.98222		50.97787	1270.56868	1.31337	33.33249
1500	7.13721	6.05028	96.93005	1131.80022	1.20672	36.00007
1486.24	7.20396		128.23126	1072.07531	1.16187	37.09981
1483.93	7.25349		150.54388	1015.08179	1.2285	35.0414
1480	7.2678	2.97105	167.01298	1001.52911	1.22334	35.1107
1465.4	7.29098		211.3693	975.70594	1.21341	35.10308
1465.22	7.29142		241.82898	975.06483	1.2132	35.10561
1460	7.29426	0.70351		971.38423	1.21183	35.03964
1400	7.32673	0.69173		929.49892	11.19571	34.28274
1280	7.39127	0.67016		847.72861	1.16112	32.772
1240	7.41278	0.66333		821.03032	1.14885	32.26891
1120	7.47759	0.65679		794.59762	1.13619	31.76595
900	7.59809	0.60943		604.41988	1.02669	27.99507
880	7.60917	0.60632		592.23888	1.01833	27.7437
820	7.63921	0.99814		554.9352	0.98473	27.19745
720	7.62059	1.0585		452.16563	0.77952	31.21428
700	7.61719	2.16441		421.67167	0.73238	32.55451
600	7.64982	0.80251		327.04394	0.62394	34.2856
520	7.67936	0.72132		266.15472	0.5478	35.47328
420	7.71658	0.64602		195.61239	0.44923	37.80282
300	7.75724	0.57492		122.39202	0.34353	40.87627
200	7.7895	0.52339		67.46756	0.26323	44.03823
120	7.81421	0.48655		27.08885	0.20505	46.97471
80	7.82621	0.46994		7.95299	0.17808	48.58644
25	7.84248	0.44669		7.95157	0.14341	50.93719

To accurately estimate the temperature distribution in the sample tested, the thermal boundary conditions should be correctly determined. The temperature t_0 of 20°C was assumed as the initial condition. The conditions of heat transfer to the environment and the copper grips in each of the zones denoted Z1 to Z5, respectively (see Fig. 3), were defined as heat fluxes q_n:

$$q_n = \alpha_e(t - t_o) \tag{7}$$

where: t_o – ambient temperature/temperature of the tool contacting the area of a specific zone, α_e– substitute heat-transfer coefficient for the specific zone.

The assumed heat transfer coefficients α were 5000 W/m^{2}K (contact interface sample-tools) and 120 W/m^{2}K (free zones of the sample) [22]. The functional model taking into account heat emission as a result of electric current flow was proposed in the form [3]:

$$Q = A(\tau)[I^2(\tau)R(T)] \tag{8}$$

where: A – intensity function selected experimentally, I – current intensity, R – resistance.

The heat emitted as a result of solidification was modeled using enthalpy-related description of the solidification with the approximation of substitute thermal capacity [31-33]. The thermal-physical characteristics, necessary for numerical simulation purposes, are collected in Table 4 [3,22].

4.Model verification-example of results

4.1. Modeling of high-temperature mechanical properties

The Direct Identification Methodology (DIM) procedure for the identification of factors in the function model of yield stress consists of four stages. The tests carried out at the first stage have the purpose of determining the characteristic temperatures of the steel tested: the solids and liquid temperatures and the zero strength temperature. For the steel S355 used in the tests, these temperatures were 1,465°C, 1,513°C, and 1,448°C, respectively. More details on determining the characteristic temperatures can be found in the monograph [3]. During the next step, based on the determined characteristic temperatures, the plan and temperature range at which the tensile tests will be conducted are selected. The experiments were conductedin accordance with the test plan shownin section 2 (stage 1st). Finally, the preliminary tests are conductedwith the support of a photogrammetric system in order to estimate the average effective working zone (20 mm). In order to calculate the nominal strain ε_n, the nominal strain rate $\dot{\varepsilon}_n$, and the nominal stress, the following formulas were used:

$$\varepsilon_n = \frac{\Delta L}{L_0} \tag{9}$$

where: ΔL - elongation (the grip stroke), L_0 - effective working zone.

$$\dot{\varepsilon}_n = \frac{s_{rate}}{L_0} \tag{10}$$

where: s_{rate} - stroke rate.

$$\sigma_n^{exp} = \frac{F}{S_0} \tag{11}$$

where: S_0 - initial cross-section area,F -tensile force.

At the fourth stage, the fundamental tensile tests are conducted in accordance with the adopted test plan. The following form of the yield stress function was assumed [3]:

$$\sigma_n^{exp} = \frac{{\varepsilon_n}^n}{\alpha} ASINH\left[\left(\frac{\dot{\varepsilon}_n}{A}\right)^m exp\left(\frac{mQ}{RT_n}\right)\right] \tag{12}$$

where: α, n, A, m, Q- model parameters,T_n - adopted test nominal temperature.

For these tests, it was assumed that the nominal temperature will be equal to the surface temperature achieved in the experiment:

$$T_n = T_{surf}^{exp} \tag{13}$$

Table 5.
The model parameters after optimization

Temperature range (°C)	α **(MPa^{-1})**	n	A **(s^{-1})**	m	Q **(J/mol)**
20 - 700	0.0018747647	0.3988701	1.25E+17	0.010061946	329831.4
700 - 1200	0.098361924	0.3494103	1.15E+17	1.065561	464576.7
1200 - 1450	0.054623641	0.2089816	1.65E+17	0.1855337	511111.2

To determine the parameters of the vector $x = (\alpha, n, A, m, Q)$ in equation (12), the optimizing module of the developed software was used, where the objective function φ was defined as follows [3]:

$$\varphi(x) = \frac{1}{N_t}\frac{1}{N_{pr}}\sum_{i=1}^{N_t}\sum_{j=1}^{N_{pr}}\left[\frac{\sigma_{n,ij}^{calc}(x) - \sigma_{n,ij}^{exp}}{\sigma_{n,ij}^{exp}}\right]^2 \tag{14}$$

where: N_t -tensile tests number, N_{pr} - number of measurement points, σ_n^{calc} - nominal stress from calculations, σ_n^{exp} -nominal stress from experiments.

In the procedure of the identification of the parameters of the vector $x = (\alpha, n, A, m, Q)$, the objective function was minimized (14). The optimization was carried out using gradient-free methods. Table 5 summarizes the identified parameters of the vector $x = (\alpha, n, A, m, Q)$ resulting from the DIM methodology. To obtain description of the experimental stress-strain relationships as accurate as possible, the temperature scope of the tests was divided into three ranges (20-700°C, 700-1,200°C, 1,200-1,450°C).

Figures 5 and 6 show examples of strain-stress curves (from experiments and calculations).The graphs include all of the points obtained by the experiment. During the execution of the experiment cycle, a growing tendency of the significant scatter of measurement data was observed. It shows, among others, huge difficulties in the execution of high-temperature experiments, despite using a modern testing unit (Gleeble 3800 simulator) dedicated to experiments of this type. Maintaining a constant test temperature was the biggest difficulty. Consequently, it resulted in a large scatter of measurement data, caused by a high sensitivity of yield stress changes to small, local temperature changes. Therefore, for the needs of the developed DIM methodology, the obtained stress-strain relationships were first subjected to smoothing, followed by the optimization procedure. Analyzing the obtained relationships (Figs. 5-6), one can observe good mapping of the characteristic of the stress change curve. The relative error range was 0.9%-8.6%.

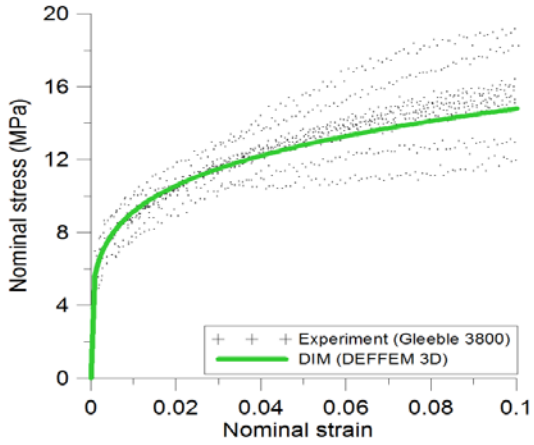

Fig. 5. Strain-stress relationships (experiment vs. calculation, T=1,300°C, nominal strain rate =0.05 s^{-1})

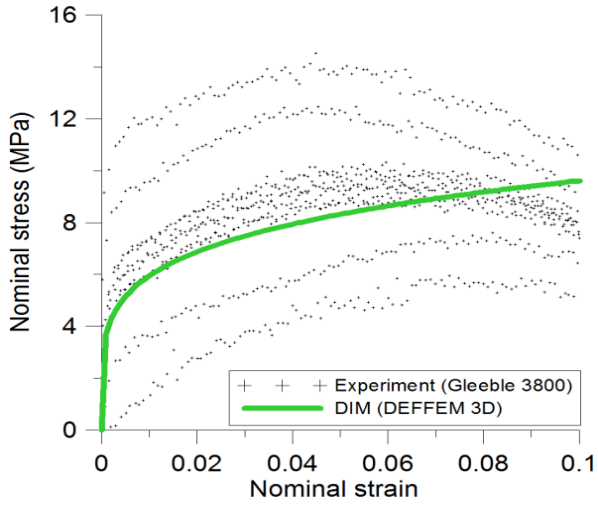

Fig. 6. Strain-stress relationships (experiment vs. calculation,T=1,450°C, nominal strain rate =0.05 s^{-1})

Figure 7 shows the calculated temperature distribution on the longitudinal section of the sample after heating to a nominal test temperature of 1,450°C. The surface temperature achieved in numerical computing according to the NTC4 numerical sensor reading was about 1,459°C, which was 9°C higher than the assumed nominal test temperature. The intensification of heat emissions resulting from the sample resistance heating occurs at the halfway point of zone Z3 (see Fig. 3-A).

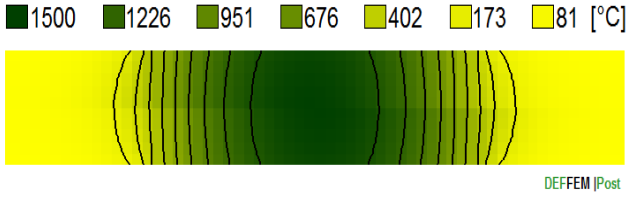

Fig. 7. Contour map of the temperature field after final heating (T=1,450°C)

Table 6 summarizes the computed temperatures for the surface (sensor NTC4) and the core (sensor NTC3) of the sample. The temperature difference between the sample surface and its core increases (readings of numerical sensors NTC4 and NTC3), when the test nominal temperature increases. The maximum core temperature of 1,500°C was received for the simulation of heating to a temperature of 1,450°C. On the other hand, in zones Z1, Z2, Z4, and Z5 (see Fig.3-A), the heat emission intensification was the lowest, while the temperature value did not exceed 300°C.

Table 6.
Summary of the computed temperatures for the surface (sensor NTC4) and the core (sensor NTC3) of the sample

Nominal temperature (°C)	**Surface temperature** (°C)	**Core temperature** (°C)	**Difference NTC4 - NTC3** (°C)
400	401.946	410.286	8.34073
700	705.530	722.779	17.2492
1100	1104.71	1135.79	31.0857
1200	1202.98	1238.13	35.1497
1250	1254.72	1292.12	37.4081
1300	1302.40	1341.93	39.5371
1350	1354.67	1396.60	41.9221
1450	1459.51	1500.24	46.7307

Publications [3, 22] present the specific results of experimental tests verifying the formulated functional model of resistance heating. The simulations were performed for temperatures from the range of 1,200°C-1,450°C, and two tool strokes, 1 and 20 mm/s. The comparison of measured and computed force values was adopted as the verification criterion. Figures 8-9 show examples of the force-stroke (from experiments and calculations). In both cases, good compatibility between the computed and measured forces was obtained. However, the nature of their changes is different. For tension simulation at a temperature of 1,450°C (when the mushy zone occurs), changes in the force are irregular. This arises from rapid changes in mechanical properties in the deformation zone, caused by local changes in the density of the solidifying sample core.

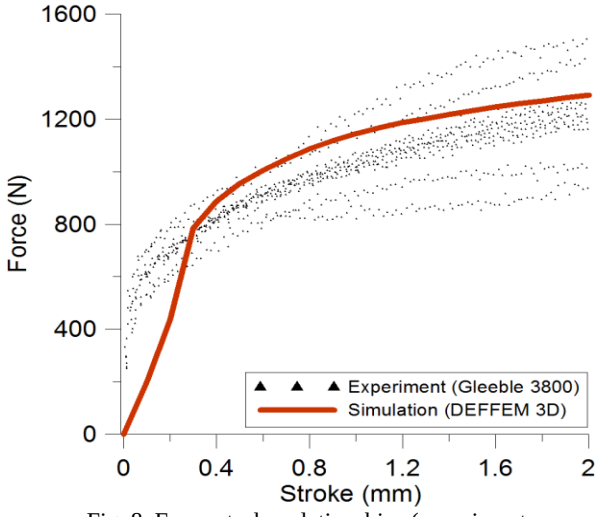

Fig. 8. Force-stroke relationships (experiment vs. calculation,T=1,350°C, nominal strain rate =1 s^{-1})

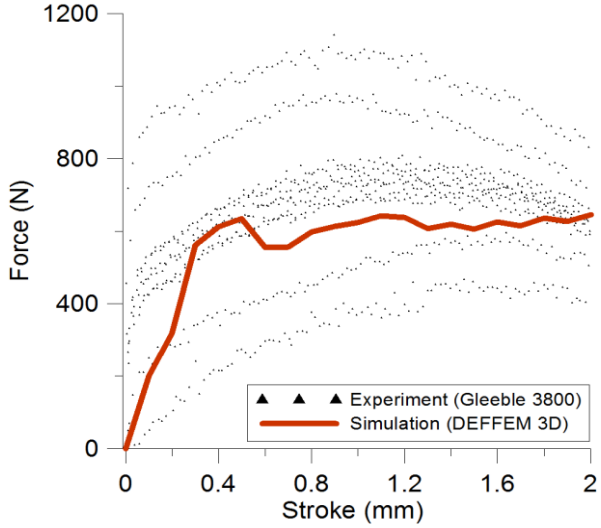

Fig. 9. Force-stroke relationships (experiment vs. calculation,*T*=1,450°C, nominal strain rate =1 s^{-1})

Table 7 summarizes the measured and computed maximum values of forces for the selected deformation temperatures. The maximum relative error was 28.5% for the test at a temperature of 1,200°C. In other cases, the relative error was within the range 3.89-15.7%.

Table 7.
Measured and computed maximum forces for selected deformation temperatures and a stroke rate of 1 and 20 mm/s

Nominal temperature (°C)	**Force** (N) **Experiment**		**Force** (N) **Simulation**		**Error** (%)	
	1 mm/s	20 mm/s	1 mm/s	20 mm/s	1 mm/s	20 mm/s
1200	1738	3143	2233	2857	28.5	9.1
1300	1422	2058	1551	1978	9.1	3.89
1350	1196	1845	1291	1703	7.9	7.69
1450	759	1057	645	1223	15.0	15.7

Figures10-11 show the distributions of strain intensity fields on the longitudinal sample section for the tests at temperatures of 1,350°C and 1,450°C. Similar to the curve of changes of force as a function of grip stroke, in this case, the intensity distributions are also different. Based on the obtained results, we can observe that, as the nominal temperature of deformation increases, the deforming zone shortens. For tension simulations at a temperature of 1,450°C, the maximum values of strain intensity on a wider cross-section cumulate, compared to the tension simulations at 1,350°C.

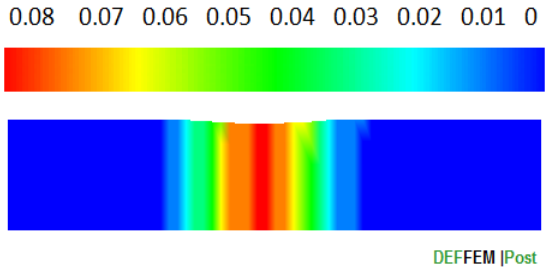

Fig. 10. The strain intensity distribution on the longitudinal sample section (T=1,350°C, stroke rate=1 mm/s)

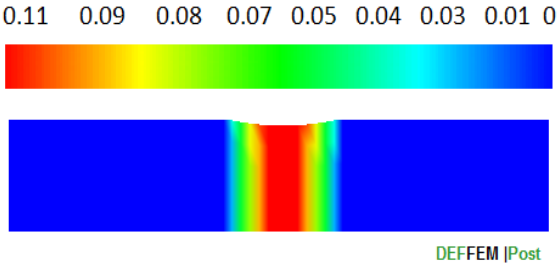

Fig. 11. The strain intensity distribution on the longitudinal sample section (T = 1,450°C, stroke rate 1 mm/s)

4.2. Modeling of the deformation zone – examples of results

The formulated yield stress model was used in simulations. The objective of the simulation was a qualitative assessment of the numerical model for the correctness of predicting the deformation zone shape. The compression process, which was carried out in accordance with the experiment plan shown in section 2, followed the resistance heating/melting/cooling process. Both for cylindrical samples (type D) and cuboidal samples (type B), as the nominal heating temperature was increasing, the temperature gradient on its cross-section was also increasing. Figure 12 shows the temperature distribution after heating the sample to a nominal temperature of 400°C. The temperature obtained in the simulation was 405.2°C (core temperature 414.8°C). In this case, the temperature gradient was about 9°C.

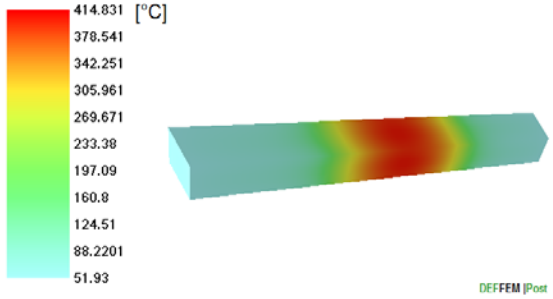

Fig. 12. Temperature distribution after heating the sample to a nominal temperature of 400°C

The maximum difference between the readings of both sensors of about 43°C was achieved in the test of heating to a nominal temperature of 1,435°C (obtained in the simulation 1,432.1°C) (Fig. 13). Analyzing the computed temperature fields shown in Figs. 12 and 13, we can observe that the intensification of heat emission resulting from the sample resistance heating occurs at the middle of the free Z2 zone (see Fig. 3-B). On the other hand, in the Z1 zone and Z3 zone (contact interface sample-grips), the intensification of heat emission was the lowest, while the temperature value did not exceed 200°C.

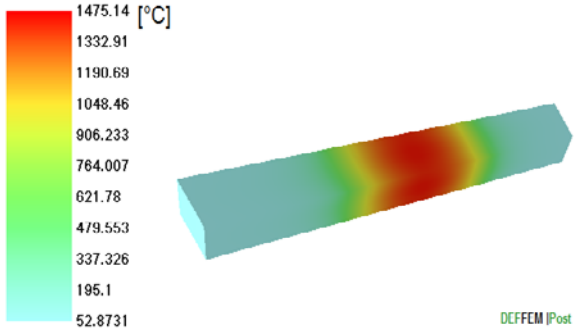

Fig. 13. Temperature distribution after heating the sample to a nominal temperature of 1,435°C (the temperature achieved in the simulation was 1,432.1°C)

After heating to a temperature of 1,435°C (core temperature 1,475°C), in the central part of the Z2 zone the mushy zone formed, being a mix of the solid and liquid phase. Figure 14 shows the examples of photos of samples compressed at a temperature of 1,300°C and 1,435°C. We can observe that, as the nominal temperature of compression increases, the deforming zone slightly shortens and the maximum cross-section dimension (on the sample axis) increases. Due to the numerical problems (large mesh distortion, no convergence of optimization procedures) occurring, numerical computing was restricted to a temperature of 1,435°C (liquid phase fraction within the sample core is 0.2).

Fig. 14. Photos of samples compressed at temperatures of 1,300°C and 1,435°C

Figure 15 shows a map of deviations for the deformation zone between finite element meshes for the samples compressed at temperatures of 1,300°C, 1,435°C. Similar to the experiment, in the case of numerical simulations we can also observe a tendency of the deforming zone to shorten and an increase in the maximum dimension of the cross-section. In the shown case (Fig. 15), there

was a 0.0005 m increase in the maximum dimension of the cross-section of the zone of the sample deformed at a temperature of 1,435°C compared to the zone of the sample deformed at 1,300°C.

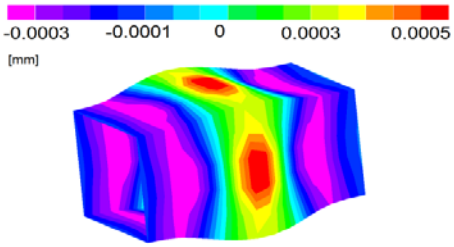

Fig. 15. Map of deviations for the deformation zone between finite element meshes (nominal temperatures of 1,300°C and 1,435°C)

For the qualitative evaluation of the spatial numerical model, three benchmarks were proposed:

1) Comparing the 3D virtual geometry of the deformation zones received by numerical calculations and the experiment. A GOM-supplied 3D ATOS Triple Scan spatial scanner was used for the digitization of the actual samples. The mapping procedure was performed using GOM Inspect V7.5SR2 software.
2) Comparison of the lengths of the deformation zones received by numerical calculations and the experiment (see Fig. 16).
3) Comparison of the maximum dimensions of the cross-sections obtained by numerical calculations and the experiment (see Fig. 16).

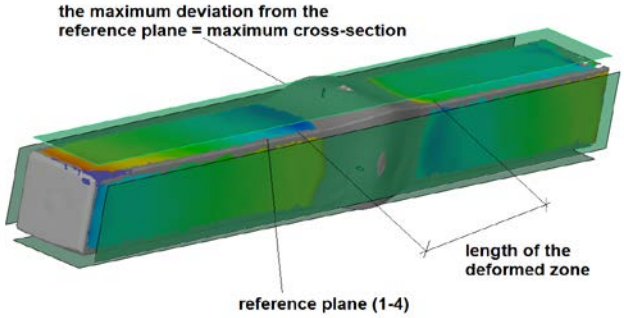

Fig. 16. Methodology of the measurement of the deformation zone executed with the ATOS Triple Scan photogrammetric system

Figure 17 shows examples of maps of deviations of the deformation zones between the finite element meshes (simulation) and the meshes obtained by digitization of actual samples. The maximum values of deviations were -0.865mm and +0.973mm, respectively. Both of the maximum values were obtained for the experiment conducted at a temperature of 1,400°C.

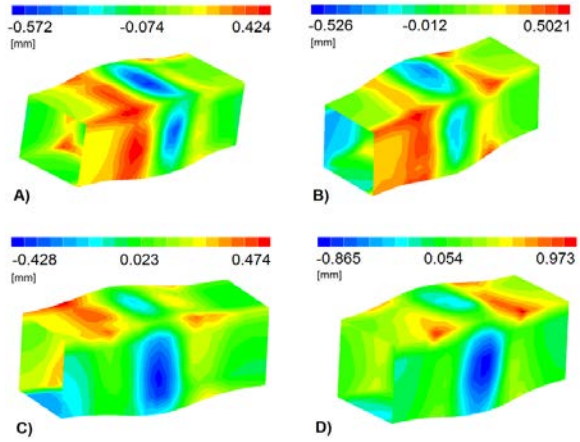

Fig. 17. Comparison of the 3D virtual geometry of the deformation zone received by numerical calculations and the experiment, A) T=1,200°C; B) T=1,300°C; C) T=1,350°C; D) T=1,400°C

Table 8 summarizes the computed and measured lengths of deformation zones and the maximum values of the cross-section dimension of the deformation zone. The maximum relative error for the criterion being the comparison of lengths of deforming zones was 16.33% for the sample compressed at a temperature of 1,435°C. For the comparison of the maximum values of the cross-section dimension, the maximum value of relative error was 7.81% for the sample deformed at 1,200°C.

Figures 18-19 show the distributions of the strain intensity for the samples compressed at temperatures of 1,300°C and 1,435°C. In both cases, the maximum strain intensity values cumulate in the centre of the sample. For the compression of the sample in the semi-solid state (surface temperature of 1,435°C, core temperature 1,475°C, solidus temperature 1,465°C), the highest values of strain intensity were obtained compared to the tests performed at lower temperatures. The contraction of the deformation zone as the test temperature increases (the mixed phase formation) is a significant factor that influences the distribution and the obtained values of strain intensity. It leads to a strong intensification of the sample core strain intensity and an increase in its maximum values.

Table 8.
Measured and calculated deformed zones and mean cross-sections for selected deformation temperatures

Nominal temperature (°C)	**Deformed zone (Gleeble)** (mm)	**Deformed zone (Simulation)** (mm)	**Error** (%)	**Mean cross-section (Gleeble)** (mm)	**Mean cross-section (Simulation)** (mm)	**Error** (%)
1200	17.790	19.234	8.11	12.758	11.761	7.81
1300	16.793	18.567	10.56	12.640	11.934	5.58
1350	16.948	18.034	6.41	12.680	12.117	4.44

1400	13.925	15.374	10.41	12.990	12.163	5.59
1435	11.450	13.328	16.33	12.854	12.028	6.43

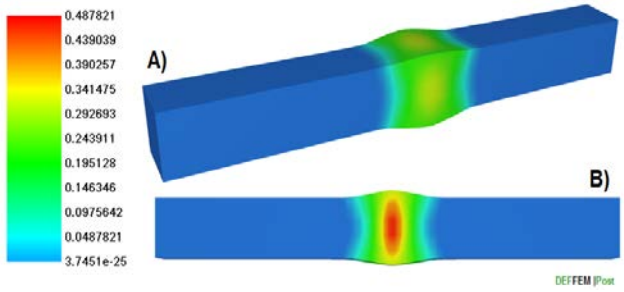

Fig. 18. Strain intensity distribution after deforming the sample at 1,300°C
(A/whole sample view, B/longitudinal section)

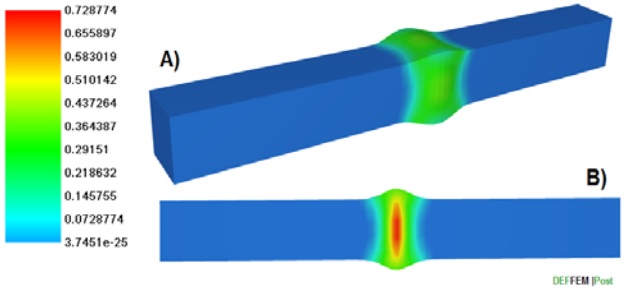

Fig. 19. Strain intensity distribution after deforming the sample at 1,435°C
(A/whole sample view, B/longitudinal section)

5. Conclusion

A spatial thermo-mechanical model based on the finite element method allowing the computer simulation of physical phenomena accompanying the steel sample testing at temperatures that are characteristic for the soft-reduction process is an original achievement presented in this paper.In the proposed solution, the power functional of the rigid-plastic solution was modified by replacing the constant volume condition with the controlled compressibility condition. It enableslocal variations of density to be included at the mechanical model level. In addition,high-temperature stress-strain relationships (temperature range up to 1,450°C) are measurable effects of the conducted work. The conducted verification simulations show the compatibility with the results obtained experimentally. The accuracy of predicting the mechanical properties on the basis of simulation fits within the relative error from 28.5% to 3.89% (experiment and numerical calculations of the process force characteristic). In the proposed methodology for predicting high-temperature stress-strain relationships, apart from the estimation of the length of the deforming zone (a 3D scanner), the value of the assumed nominal test temperature is a significant parameter. Bear in mind that the temperature within the sample volume centeris by a few orders of magnitude higher than the assumed nominal test temperature. The maximum temperature difference between the sample surface and its core of 46.73°C was achieved during heating to the nominal test temperature of 1,450°C. Therefore, we can conclude that a modification of the DIM methodology, taking into account the methodology of inverse computing combined with multi-scale modeling for the identification of factors in the rheological model of the steel examined will enableus to obtain more accurate results. For numerical simulations using the spatial model, the accuracy of the prediction of the shape and dimensions of the strain zone fits within the relative error from 6.41% to 16.33% (deformed zone length), 4.44%-7.81% (mean cross-section), and maximum deviations -0.865/+0.973 mm between the geometry of the mesh obtained by simulation and the mesh obtained from a 3D scanner (actual sample). The simulation of deformation at a temperature of 1,450°C failed.Numerical problems such as high mesh distortions and no convergence of optimization algorithms allowed us to define the limitations in the application of the developed 3D model to the maximum test temperature of 1,435°C (sample core temperature of 1,475°C) or liquid phase fraction $f_l \leq 0.2$.

Acknowledgment

1. The research work has been supported by the Polish National Science Centre, Decision number: DEC-2011/03/D/ST8/04041.
2. The work was realized as a part of fundamental research financed by the Ministry ofScience and Higher Education, grant no. 16.16.110.663.

References

[1] Haga, T. & Suzuki, S.(2003). Study on high-speed twin-roll caster for aluminum alloys. *Journal of Materials Processing Technology*. 144(1), 895-900. DOI: 10.1016/S0924-0136(03)00400-X.
[2] Haga, T., Tkahashi, K., Ikawa, M., et al. (2004). Twin roll casting of aluminum alloy strips. *Journal of Materials Processing Technology*. 154(2), 42-47. DOI: 10.1016/j.jmatprotec.2004.04.018.
[3] Hojny, M. (2018).*Modeling steel deformation in the semi-solid state*. Switzerland: Springer.
[4] Zhang, L., Shen, H., Rong, Y., et al. (2007). Numerical simulation on solidification and thermal stress of continuous casting billet in mold based on meshless methods. *Materials Science and Engineering*. 466(1-2), 71-78. DOI: 10.1016/j.msea.2007.02.103.
[5] Kalaki, A. & Ketabchi, M. (2013). Predicting the rheological behavior of AISI D2 semi-solid steel by plastic instability approach. *American Journal of Materials Engineering and Technology*. 1(3), 41-45. DOI: 10.12691/materials-1-3-3.
[6] Hassas-Irani, S.B., Zarei-Hanzaki, A., Bazaz, B., Roostaei, A. (2013). Microstructure evolution and semi-solid deformation behavior of an A356 aluminum alloy processed by strain induced melt activated method. *Materials and Design*. 46, 579-587. DOI: 10.1016/j.matdes.2012.10.041.

[7] Zhang, C., Zhao, S., Yan, G., Wang, Y. (2018). Deformation behaviour and microstructures of semi-solid A356.2 alloy prepared by radial forging process during high solid fraction compression. *Journal of Engineering Manufacture*. 232(3), 487, 498.
[8] Wang, J. (2016). Deformation Behavior of Semi-Solid ZCuSn10P1 Copper Alloy during Isothermal Compression. *Solid State Phenomena*. 256, 31-38.
[9] Shashikanth, C.H. & Davidson, M.J. (2015). Experimental and simulation studies on thixoforming of AA 2017 alloy. *Mat. at High Temperatures*. 32(6), 541-550. DOI: 10.1179/1878641314Y.0000000043.
[10] Bharath, K., Khanra, A.K., Davidson, M.J. (2019). *Microstructural Analysis and Simulation Studies of Semi-solid Extruded Al–Cu–Mg Powder Metallurgy Alloys* (pp.101-114). Advances in Materials and Metallurgy:Springer.
[11] Kang, C.G. & Yoon, J.H. (1997). A finite-element analysis on the upsetting process of semi-solid aluminum material. *Journal of Materials Processing Technology*. 66(1-3), 76-84. DOI: 10.1016 / S0924-0136 (96) 02498-3.
[12] Hostos, J.C.A., et al. (2018). Modeling the viscoplastic flow behavior of a 20MnCr5 steel grade deformed under hot-working conditions, employing a meshless technique. *International Journal of Plasticity*. 103, 119-142. DOI: 10.1016/j.ijplas.2018.01.005.
[13] Kopp, R., Choi, J. & Neudenberger, D. (2003). Simple compression test and simulation of an Sn–15% Pb alloy in the semi-solid state. *Journal of Materials Processing Technology*. 135(2), 317-323. DOI: 10.1016/S0924-0136(02)00863-4.
[14] Modigell, M., Pape, L. & Hufschmidt, M. (2004). The Rheological Behaviour of Metallic Suspensions. *Steel Research International*. 75(3), 506-512. DOI: 10.1002/ srin.200405803.
[15] Hufschmidt, M., Modigell, M. & Petera, J. (2004). Two-Phase Simulations as a Development Tool for Thixoforming Processes. *Steel Research International*. 75(3), 513-518. DOI: 10.1002/srin.200405804.
[16] Jing, Y.L., Sumio, S. & Jun, Y. (2005). Microstructural evolution and flow stress of semi-solid type 304 stainless steel. *Journal of Materials Processing Technology*. 161(3), 396-406. DOI: 10.1016/j.jmatprotec.2004.07.063.
[17] Jin, S.D. & Hwan, O.K. (2002). Phase-field modelling of the thermo-mechanical properties of carbon steels. *Acta Materialia*. 50, 2259-2268. DOI: 10.1016/S1359-6454(02)00012-5.
[18] Xiao, C., et al. (2013). Optimization Investigation on the Soft Reduction Parameters of Medium Carbon Microalloy. *Materials Processing Fundamentals*. Springer. 109-116. DOI: 10.1007/978-3-319-48197-5_12.
[19] Han, Z., et al. (2010). Development and Application of Dynamic Soft-reduction Control Model to Slab Continuous Casting Process. *ISIJ International*. 50(11), 1637-1643. DOI: 10.2355/isijinternational.50.1637.
[20] Li, Y., Li, L. & Zhang, J. (2017). Study and application of a simplified soft reduction amount model for improved internal quality of continuous casting. *Steel Research International*. 88(12), 1700176-1700219. DOI: 10.1002/srin.201700176.
[21] Bereczki, P., et al. (2015). Different applications of the gleeble thermal–mechanical simulator in material testing, technology optimization, and process modeling. *Materials Performance and Characterization 4*. No. 3, 399-420. DOI: 10.1520/ MPC20150006.
[22] Hojny, M., et al. (2019). Multiscale model of heating-remelting-cooling in the Gleeble 3800 thermo-mechanical simulator system. *Archives of Metallurgy and Materials*. 64(1), 401-412. DOI: 10.24425 / amm.2019.126266.
[23] Pieja, T., et al. (2017). *Numerical analysis of cooling system in warm metal forming process* (pp. 261-266). Brno, Czech: Proceedings of the Metal.
[24] Hojny, M. (2013). Thermo-mechanical model of a TIG welding process for the aircraft industry. *Archives of Metallurgy and Materials*. 58(4), 1125-1130.DOI: 10.2478/amm-2013-0136.
[25] Hu, D. & Kovacevic, R. (2003). Sensing, modeling and control for laser-based additive manufacturing. *Journal of Machine Tools & Manufacture*. 43, 51-60. DOI: 10.1016/S0890-6955(02)00163-3.
[26] Ba Lan, T., et al. (2017). A new route for semi-solid steel forging. *Manufacturing Technology*. 66(1), 297-300. DOI: 10.1016/j.cirp.2017.04.111.
[27] Głowacki, M. (2005). The mathematical modelling of thermo-mechanical processing of steel during multi-pass shape rolling. *Journal of Materials Processing Technology*. 168, 336-343. DOI: 10.1016/j.jmatprotec.2004.12.007.
[28] Lliboutry, L.A. (1987). *The rigid-plastic model, Mechanics of Fluids and Transport Processes* (pp. 379-410). Dordrecht: Springer.
[29] Lenard, J.G., Pietrzyk, M., Cser, L. (1999). *Mathematical and physical simulation of the properties of hot rolled products.*Amsterdam: Elsevier.
[30] Głowacki, M. (2012). *Mathematical modeling and computer simulations of metal deformation - theory and practice* (pp. 229-238). Kraków: AGH. (in Polish).
[31] Jonsta. P., et al. (2015). Contribution to the thermal properties of selected steels. *Metalurgija*. 54(1), 187-190.
[32] Szyczgioł, N. (1997). Równania krzepnięcia w ujęciu metody elementów skończonych. *Solidification of Metals and Alloys.* 30, 221-232.
[33] Lewis, R.W, Roberts, P.M. (1987). Finite element simulation of solidification problems. *Applied Scientific Research*. 44, 61-92. DOI: 10.1007/978-94-009-3617-1_6.